Materials Advances

PAPER

Check for updates

Realization of the dehydrogenation pathway of formic acid oxidation by ultra-small core–shell Au–Pt nanoparticles with discrete Pt shells†

Yi Cao,‡[a] Xiang Zhang,‡[a] Xinru Yue,[a] Mengmeng Zhang,[a] Wei Du [ID][b] and Haibing Xia [ID] *[a]

In this work, ultra-small core–shell Au–Pt nanoparticles with discrete Pt shells (denoted as USCS$_D$ Au–Pt NPs) were successfully prepared by Fe(II)-assisted one-pot co-reduction of Au(III) ions and an ultra-low concentration of Pt(II) ions in citrate solution. In the as-prepared USCS$_D$ Au–Pt NPs, the Pt atoms on their outer surfaces are effectively isolated by Au atoms (denoted as a discrete shell, CS$_D$). Furthermore, the as-prepared USCS$_D$ Au–Pt NPs are determined to be USCS$_D$ Au$_{61.2}$@Au$_{27.3}$Pt$_{11.5}$ NPs with an average size of 2.3 nm using a number of characterization techniques, including transmission electron microscopy (TEM), energy dispersive X-ray spectroscopy (EDS), cyclic voltammetry (CV), CO stripping voltammetry and X-ray photoelectron spectroscopy (XPS). Moreover, the as-prepared USCS$_D$ Au$_{61.2}$@Au$_{27.3}$Pt$_{11.5}$-NP/C catalysts towards the formic acid oxidation reaction (FAOR) proceed through the direct pathway (dehydrogenation). In addition, their mass activity and specific activity towards the FAOR are 6.91 A mg$_{Pt}^{-1}$ and 4.88 mA cm^{-2}, which are about 16.8 and 7.33 times higher than those (0.4 A mg$_{Pt}^{-1}$ and 0.67 mA cm^{-2}) of commercial Pt/C catalysts, respectively.

1. Introduction

It is well known that the catalytic performance of electrocatalysts is highly dependent on their composition, structure and morphology.[1–3] Moreover, the same electrocatalysts may show different catalytic performances for different reactions. For instance, in our previous work, ultra-small core–shell Au–Pt nanoparticles (denoted as USCS Au–Pt NPs) with Au-decorated Pt surfaces were successfully prepared.[4] Furthermore, they exhibited improved electrocatalytic performance towards the HER and ORR in acidic media, compared with commercial Pt/C catalysts. However, their performance towards the formic acid oxidation reaction (FAOR) is not satisfactory (Fig. S1, ESI†). In the as-prepared USCS Au–Pt NPs, Pt atoms on the outer surfaces are almost continuous and doped with a small fraction of Au atoms, which are demonstrated by their CO stripping voltammograms. Accordingly, they exhibit strong adsorption toward the CO species, which are the main intermediates produced from the indirect

pathway (dehydration of formic acid) in the FAOR, thus leading to the loss of active sites on the surfaces.[5–10]

Meanwhile, it is known that Au has good anti-poison ability to CO.[11–13] Therefore, continuous Pt atoms on the outer surfaces are well dispersed by a high fraction of Au atoms, which would display an improved anti-poison ability to CO due to the decreasing density of Pt atoms and the presence of Au atoms.[14–17] In addition, the formation of atomically dispersed Pt atoms on the outer surfaces of Au–Pt NPs would promote the direct pathway (dehydrogenation of formic acid), thus improving the catalytic performance towards the FAOR.[18–20] Note that although Au would not directly involve the FAOR, the presence of Au can improve the anti-poison ability of Pt to CO and further enhance their FAOR performance.

In this work, ultra-small core–shell structured Au–Pt nanoparticles with discrete Pt shells (denoted as USCS$_D$ Au–Pt NPs) were first synthesized on the basis of our previous work (Scheme 1).[4] Accordingly, USCS Au$_{38.4}$@Au$_{9.3}$Pt$_{52.3}$ NPs with Pt-rich shells obtained in previous work (Schemes 1b and d) can become USCS$_D$ Au$_{61.2}$@Au$_{27.3}$Pt$_{11.5}$ NPs with Au-rich shells (Schemes 1c and e) by just reducing the concentration of Pt(II) ions in the reaction mixture solution in the presence of citrate and Fe ions (Scheme 1a), since the concentration of Au(III) ions remains constant and the number and size of *in situ* Au cores also keep unchanged. In our case, due to the weaker reducing ability of citrate, Fe(II) ions and citrate ions mainly act as the
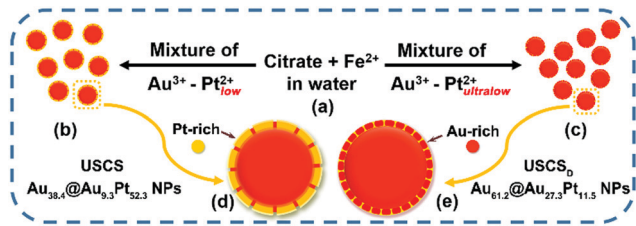
[a] *State Key Laboratory of Crystal Materials, Shandong University, Jinan, 250100, P. R. China. E-mail: hbxia@sdu.edu.cn*

[b] *School of Environment and Material Engineering, Yantai University, Yantai 264005, P. R. China*

‡ These authors contributed equally.

Scheme 1 Schematic depiction of the synthetic procedure of $USCS_D$ Au–Pt NPs by Fe(II)-assisted one-pot co-reduction of Au(III) ions and an ultralow concentration of Pt(II) ions in the citrate solution. (a) Reaction mixture containing citrate and Fe^{3+} ions. (b) Formation of USCS $Au_{38.4}@Au_{9.3}Pt_{52.3}$ NPs. (c) Formation of $USCS_D$ $Au_{61.2}@Au_{27.3}Pt_{11.5}$ NPs. (d) Magnified model of one USCS $Au_{38.4}@Au_{9.3}Pt_{52.3}$ NP. (e) Magnified model of one $USCS_D$ $Au_{61.2}@Au_{27.3}Pt_{11.5}$ NPs.

reductant and the stabilizer, respectively.[4] The optimal concentration of Pt(II) ions for the formation of $USCS_D$ $Au_{61.2}@Au_{27.3}Pt_{11.5}$ NPs with optimal electrocatalytic performance towards the formic acid oxidation reaction (FAOR) in acidic media was investigated in an ultralow concentration range. Then, the size, composition and structure of the as-prepared $USCS_D$ $Au_{61.2}@Au_{27.3}Pt_{11.5}$ NPs were characterized by transmission electron microscopy (TEM), energy dispersive X-ray spectroscopy (EDS), cyclic voltammetry (CV), CO stripping voltammetry and X-ray photoelectron spectroscopy (XPS) measurements. Lastly, the electrocatalytic performance of $USCS_D$ $Au_{61.2}@Au_{27.3}Pt_{11.5}$ NP/C catalysts ($USCS_D$ $Au_{61.2}@Au_{27.3}Pt_{11.5}$ NPs loaded on carbon black) as well as commercial Pt/C catalysts and USCS $Au_{38.4}@Au_{9.3}Pt_{52.3}$-NP/C catalysts towards the FAOR was investigated in acidic media for comparison.

2. Experimental

2.1 Synthesis of $USCS_D$ Au–Pt NPs

$USCS_D$ $Au_{61.2}@Au_{27.3}Pt_{11.5}$ NPs with discrete Pt shells were prepared as follows. Firstly, 1.0 mL of sodium citrate (1 wt%) and 130 μL of $FeSO_4 \cdot 7H_2O$ (0.05 M) were sequentially added into 47.0 mL of boiling water in a two-neck bottle, followed by the quick addition of 2.0 mL of the mixture solution containing $HAuCl_4$ (30 μL, 1 wt%) and K_2PtCl_4 (4 μL, 1 wt%), which was premixed just for 1 minute at room temperature before its addition. Then, the above mixture solution in the two-neck bottle was further boiled for 30 minutes with stirring to confirm the formation of uniformly quasi-spherical $USCS_D$ $Au_{61.2}@Au_{27.3}Pt_{11.5}$ NPs. Eventually, the color of the reaction mixture solution in the two-neck bottle was pale yellow. In our case, Fe(II) ions are oxidized into Fe(III) ions by Pt(II) ions and Au(III) ions. Accordingly, the Fe species in the solution would be Fe(III) ions and the remaining Fe(II) ions. Therefore, there is hardly any Fe species in the final $USCS_D$ $Au_{61.2}@Au_{27.3}Pt_{11.5}$ NPs. Moreover, both Fe(III) ions and Fe(II) ions can be washed away during the fabrication of $USCS_D$ $Au_{61.2}@Au_{27.3}Pt_{11.5}$-NP/C catalysts. For the sake of a better comparison with commercial Pt/C catalysts, the as-prepared $USCS_D$ $Au_{61.2}@Au_{27.3}Pt_{11.5}$ NPs were also loaded onto carbon black (Cabot, Vulcan XC-72R)

with a Pt loading of ∼20% as catalysts (named $USCS_D$ $Au_{61.2}@Au_{27.3}Pt_{11.5}$-NP/C catalysts). The detailed preparation procedure is as follows. Firstly, the suspension of carbon black post-treatment was added into the dispersion solution of $USCS_D$ $Au_{61.2}@Au_{27.3}Pt_{11.5}$ NPs, followed by ultrasonication for 1 h at room temperature and centrifugation treatment twice (at 10000 rcf for 10 min) and drying at 80 °C.

2.2 Electrochemical measurements

Before the FAOR test, all the electrolytes were purged with N_2 for 30 min and bubbled all the time during the whole test. Cyclic voltammetry (CV) curves were first recorded in a N_2-saturated 0.25 M H_2SO_4 solution with and without 1.0 M HCOOH by cycling between −0.22 and 1.48 V (vs. Ag/AgCl) at a scan rate of 50 mV s^{-1}. The chronoamperometric (CA) tests of all the catalysts were performed at 0.3 V (vs. Ag/AgCl) in a N_2-saturated 0.25 M H_2SO_4 solution containing 1.0 M HCOOH for 1000 s.

3. Results and discussion

3.1 Synthesis and characterization of $USCS_D$ $Au_{61.2}@Au_{27.3}Pt_{11.5}$ NPs

Firstly, a series of concentrations of Pt(II) ions were investigated in the ultralow concentration range between 1.46 and 2.43 μM for synthesis of $USCS_D$ Au–Pt NPs on the basis of our previously reported procedure.[4] After their successful preparation, the as-prepared Au–Pt NPs were loaded on Vulcan XC-72R carbon black as catalysts for evaluation of their electrocatalytic performance towards the FAOR. In these tests, their forward scanning voltammograms were measured in the potential range of −0.2 to 1.0 V (vs. Ag/AgCl) and their mass activity was normalized by the amount of Pt loaded on the working electrode (Fig. 1). The dehydrogenation and dehydration of formic acid are named the direct pathway and indirect pathway, respectively. Although the final products obtained through the two pathways are the same (CO_2), the active intermediates are totally different.
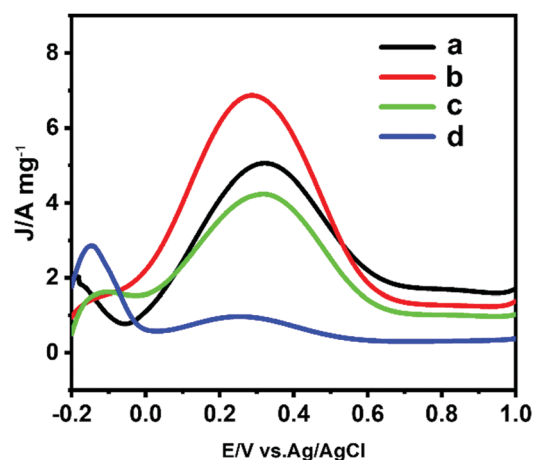

Fig. 1 Mass-normalized current density towards the FAOR of a series of Au–Pt NP/C catalysts prepared at different Pt(II) ion concentrations: 2.43 μM (a), 1.95 μM (b), 1.70 μM (c), and 1.46 μM (d).

HCOOH is directly electrooxidized into CO_2 *via* the active intermediates ($HCOO_{ads}$) through the direct pathway, while HCOOH is electrooxidized into CO_2 *via* CO_{ads} through the indirect pathway. Since Pt has a strong absorption ability to CO, the low ratio of Pt on the surfaces of the $USCS_D$ Au–Pt NP/C catalysts would favor the occurrence of the FAOR through the direct pathway, instead of through the indirect pathway. Meanwhile, the peak potentials in the CV curves of the FAOR through the different pathways should be different. Moreover, the FAORs through the two pathways occur simultaneously and are competitive. Therefore, the main pathway during the FAOR can be identified by the relative peak intensity at the two potentials for the occurrence of the FAOR through the direct pathway and the indirect pathway. Accordingly, the CV curves of the FAOR with peak potentials centered at about 0.28 V should follow the direct pathway (Fig. 1), while those with peak potentials centered at about 0.7–0.8 V should follow the indirect pathway (Fig. S1, ESI†).[21–23] It can be seen that, with the decrease of the concentration of Pt(II) ions, their mass activity first increases from 5.12 to 6.91 A mg_{Pt}^{-1} and then decreases to 4.24 and 0.98 A mg_{Pt}^{-1} (Fig. 1 and Table S1, ESI†). Thus, the $USCS_D$ Au–Pt–NP/C catalysts prepared at a concentration of Pt(II) ions of 1.95 μM (sample b in Fig. 1) show the largest mass activity. As for the same type of FAOR, the catalysts have the largest mass-normalized current density towards the FAOR, indicating that they display optimal performance. Accordingly, the optimum Pt precursor content should be the one used for their synthesis. Thus, the optimum Pt precursor content is 1.95 μM.

In the low magnification TEM images, the as-prepared $USCS_D$ $Au_{61.2}@Au_{27.3}Pt_{11.5}$ NPs are well-dispersed (Fig. 2a and b) and display a relatively broad particle size distribution (Fig. 2f). Furthermore, the as-prepared $USCS_D$ $Au_{61.2}@Au_{27.3}Pt_{11.5}$ NPs with an average size of about 2.3 nm show clear lattice fringes in the high-resolution TEM image (inset in

Fig. 2c), indicating their highly crystalline state.[24,25] In addition, the lattice spacing is 0.234 nm, which is slightly smaller than that (0.236 nm) of the Au(111) plane due to the presence of Pt.

In addition, on the basis of the EDS results of $USCS_D$ $Au_{61.2}@Au_{27.3}Pt_{11.5}$-NP/C catalysts (Fig. 2d and e), the molar ratio of Pt to Au is about 0.13 (11.5% Pt and 88.5% Au, respectively), which is basically the same as that of Pt precursor-to-Au precursor (0.130). Note that, due to its ultra-small size and the detection limit of HAADF-STEM-EDS mapping, the cross-sectional compositional line profile of a single $USCS_D$ $Au_{61.2}@Au_{27.3}Pt_{11.5}$ NP cannot be obtained.

3.2 Difference between USCS $Au_{38.4}@Au_{9.3}Pt_{52.3}$ NPs and $USCS_D$ $Au_{61.2}@Au_{27.3}Pt_{11.5}$ NPs

To be honest, it is hard to differentiate between USCS $Au_{38.4}@Au_{9.3}Pt_{52.3}$ NPs and $USCS_D$ $Au_{61.2}@Au_{27.3}Pt_{11.5}$ NPs. Fortunately, the electrochemical measurement is a surface-sensitive testing method, which allows us to identify the difference between them. On the basis of their CVs (Fig. S2, ESI†), their ECSA values were calculated accordingly, which are shown in Fig. 3 and listed in Table S1, ESI.† Since the ECSA value of the USCS Au@Pt NPs is mass-normalized by Pt mass, it would continuously increase before the Au cores are fully covered by one layer of Pt atoms in general. One can clearly see that when the concentration of Pt(II) ions is below 1.95 μM, their ECSA value linearly increases with the increasing concentration of Pt(II) ions (solid points on the dotted line in Fig. 3). When the concentration of Pt(II) ions reaches 2.43 μM, the real ECSA value (separate solid points) is below the theoretical one (the red point on the dotted line in Fig. 3). These results indicate that the surfaces of the as-prepared $USCS_D$ $Au_{61.2}@Au_{27.3}Pt_{11.5}$ NPs are not fully covered by Pt atoms when the concentration of Pt(II) ions is below 1.95 μM. In a word, the Pt atoms on their surfaces are in a certain degree of discontinuity.

CO stripping voltammetry of commercial Pt/C catalysts, USCS $Au_{38.4}@Au_{9.3}Pt_{52.3}$-NP/C catalysts and $USCS_D$ $Au_{61.2}@Au_{27.3}Pt_{11.5}$-NP/C catalysts was further carried out to illustrate the formation of discrete Pt shells by comparison
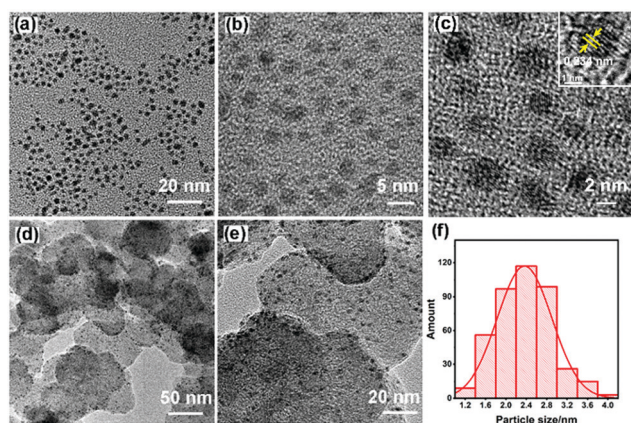

Fig. 2 Low magnification (a and d), high magnification (b and e), and high-resolution (c) TEM images of the $USCS_D$ $Au_{61.2}@Au_{27.3}Pt_{11.5}$ NPs (a, b and c) and $USCS_D$ $Au_{61.2}@Au_{27.3}Pt_{11.5}$-NP/C (d and e), and their histograms of particle size distribution (f). The concentrations of Fe(II) ions, Au(III) ions, citrate, and Pt(II) ions used for the synthesis of $USCS_D$ $Au_{61.2}@Au_{27.3}Pt_{11.5}$ NPs were 0.130, 0.015, 0.687 mM, and 1.95 μM, respectively.
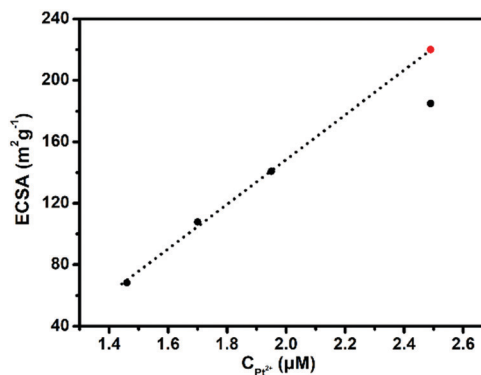

Fig. 3 The real (black points) and the theoretical value (red point) of the calculated ECSA values of $USCS_D$ Au–Pt–NP/C catalysts prepared at different concentrations of Pt(II) ions from 1.46 μM to 1.70 μM, 1.95 μM, and 2.43 μM.
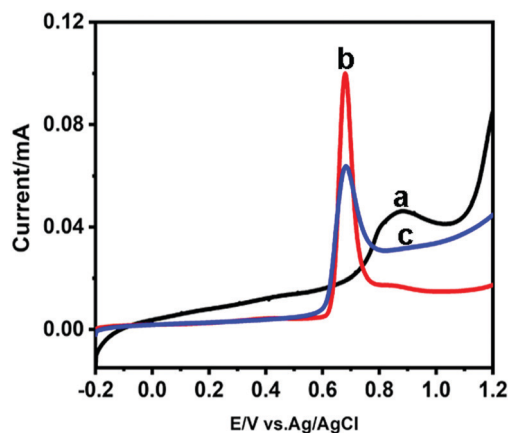
Fig. 4 CO stripping voltammograms of $USCS_D$ $Au_{61.2}@Au_{27.3}Pt_{11.5}$-NP/C catalysts (a), commercial Pt/C catalysts (b) and USCS $Au_{38.4}@Au_{9.3}Pt_{52.3}$-NP/C catalysts (c).
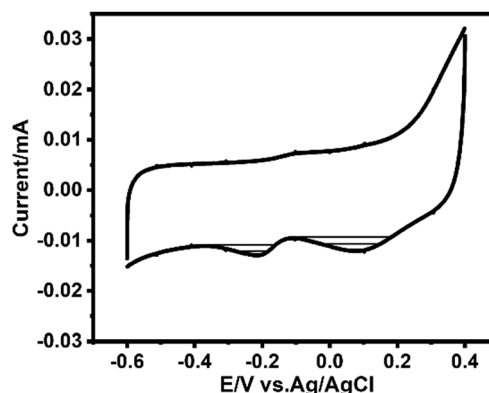

Fig. 5 CV curves of $USCS_D$ $Au_{61.2}@Au_{27.3}Pt_{11.5}$ NPs measured in the presence of N_2-saturated 0.3 M KOH solution. The area covered by the horizontal line is used to calculate the relative contents of platinum and gold on their surface by using the surface charge related to the reduction of oxide species.

(Fig. 4). Clearly, both the commercial Pt/C catalysts and USCS $Au_{38.4}@Au_{9.3}Pt_{52.3}$-NP/C catalysts show pronounced and sharp CO oxidation peaks (red and blue curves in Fig. 4). In addition, their positions are both centered at about ∼0.7 V. These results indicate that USCS $Au_{38.4}@Au_{9.3}Pt_{52.3}$-NP/C catalysts are fully covered by Pt atoms and have a strong adsorption ability for CO. In contrast, the CO oxidation peak of $USCS_D$ $Au_{61.2}@Au_{27.3}Pt_{11.5}$-NP/C catalysts is more diffused from −0.1 to 1.05 V, accompanied by a broader peak from 0.7 to 1.05 V caused by electronic effects between the Au-core and discrete Au-rich Pt shell (the black curve in Fig. 4).[10] The results further indicate that the Pt atoms on the surface of the $USCS_D$ $Au_{61.2}@Au_{27.3}Pt_{11.5}$ NPs are not continuous and have a weak adsorption ability for CO, which is consistent with those reported in the literature.[26]

However, the large potential range of the CO-stripping peak of $USCS_D$ $Au_{61.2}@Au_{27.3}Pt_{11.5}$-NP/C catalysts would offset the decreasing adsorption ability for CO due to the increasing amount of adsorption sites, which is indicated by the presence of a broad adsorption potential range for CO (from −0.1 to 1.05 V).[10,27] That is, $USCS_D$ $Au_{61.2}@Au_{27.3}Pt_{11.5}$-NP/C catalysts would promote the desorption of intermediate products in the catalytic process towards the FAOR due to the decreasing adsorption ability and make them convert to the direct pathway, thereby enhancing the FAOR catalytic performance.[7]

3.3. Determination of the elemental composition of $USCS_D$ $Au_{61.2}@Au_{27.3}Pt_{11.5}$ NPs

According to the method reported in our previous work,[4,28–31] the bulk composition and surface composition of the $USCS_D$ Au–Pt NPs can also be determined by cyclic voltammetry in alkaline media. The surface composition of the as-prepared $USCS_D$ Au–Pt NPs can be calculated on the basis of the surface areas of Au and Pt obtained, which can be deduced as follows:

$$m = \frac{S_{Pt}}{S_{Pt} + S_{Au}}100$$

where m represents the Pt content and S_{Pt} and S_{Au} are the surface areas covered by Pt and Au oxides, respectively.

Accordingly, the atomic fractions of elemental Pt and elemental Au in the shell and Au in the core of the as-prepared $USCS_D$ Au–Pt NPs were determined to be 11.5 at%, 27.3 at%, and 61.2 at%, respectively, based on the results from their CVs (Fig. 5 and Fig. S3 and Table S2, ESI†). Thus, the composition of the as-prepared $USCS_D$ Au–Pt NPs was determined to be $USCS_D$ $Au_{61.2}@Au_{27.3}Pt_{11.5}$ NPs, which have the CS structure with an Au core and a discrete Pt shell.

3.4 XPS characterization of $USCS_D$ $Au_{61.2}@Au_{27.3}Pt_{11.5}$ NPs

The chemical states of elemental Pt and elemental Au in $USCS_D$ $Au_{61.2}@Au_{27.3}Pt_{11.5}$ NP/C catalysts were further studied by XPS (Fig. 6). On the one hand, the Pt 4f signals in the XPS spectra of $USCS_D$ $Au_{61.2}@Au_{27.3}Pt_{11.5}$-NP/C catalysts are similar to those of commercial Pt/C catalysts (Fig. 6A and B), except that their peak intensity is rather weak due to their low Pt content (Fig. 6A). In addition, the peaks located at 71.4 and 74.5 eV belong to the $4f_{7/2}$ and $4f_{5/2}$ signals of metallic Pt(0), while the peaks located at 73.0 and 76.1 eV belong to the $4f_{7/2}$ and $4f_{5/2}$ signals of Pt(ɪɪ) oxide, respectively. Based on the de-convolution XPS results, the $USCS_D$ $Au_{61.2}@Au_{27.3}Pt_{11.5}$-NP/C catalysts are composed of 48% metallic Pt(0) and 52% Pt(ɪɪ) oxide. On the other hand, the binding energy (BE) of metallic Pt(0) $4f_{7/2}$ in the $USCS_D$ $Au_{61.2}@Au_{27.3}Pt_{11.5}$-NP/C catalysts is 71.4 eV, which is negatively shifted about 0.7 eV than that (72.1 eV) of commercial Pt/C catalysts (Fig. 6A and B and Table S3, ESI†).

Meanwhile, the BEs of Au(0) $4f_{7/2}$ and $4f_{5/2}$ in $USCS_D$ $Au_{61.2}@Au_{27.3}Pt_{11.5}$-NP/C catalysts are 84.3 and 88.0 eV, respectively, which are both negatively shifted about 0.1 eV than those (84.4 and 88.1 eV) of Au–NP/C catalysts (Fig. 6C and D and Table S4, ESI†). In our previous work, the Au 4f signals and Pt 4f signals in the XPS spectra of USCS $Au_{38.4}@Au_{9.3}Pt_{52.3}$-NP/C catalysts show a negative shift and a positive shift, respectively (Fig. S4, ESI†). However, both the Pt and Au 4f signals in the XPS spectra of $USCS_D$ $Au_{61.2}@Au_{27.3}Pt_{11.5}$-NP/C catalysts show
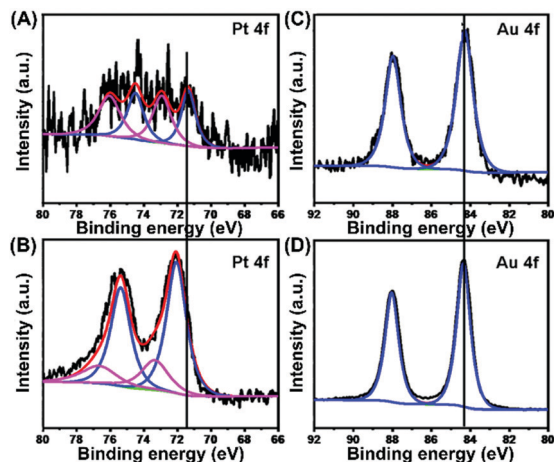
Fig. 6 High-resolution XPS spectra of the Pt 4f signals in the USCS$_D$ Au$_{61.2}$@Au$_{27.3}$Pt$_{11.5}$-NP/C catalysts (A) and commercial Pt/C catalysts (B), and those of the Au 4f signals in USCS$_D$ Au$_{61.2}$@Au$_{27.3}$Pt$_{11.5}$-NP/C catalysts (C) and Au-NP/C catalysts (D).

negative shifts. These results indicate that USCS$_D$ Au$_{61.2}$@Au$_{27.3}$Pt$_{11.5}$-NP/C catalysts contain Au–Pt alloyed surfaces.[32–34] Furthermore, the Pt atoms on their Au–Pt alloyed surfaces are isolated by Au atoms due to the ultralow Pt content, combined with the results above.

3.5 Electrocatalytic performance of USCS$_D$ Au$_{61.2}$@Au$_{27.3}$Pt$_{11.5}$-NP/C catalysts towards the FAOR

The electrocatalytic performance of the as-prepared USCS$_D$ Au$_{61.2}$@Au$_{27.3}$Pt$_{11.5}$-NP/C catalysts towards the FAOR in acidic media was investigated as well as that of commercial Pt/C catalysts (Johnson Matthey, 20 wt%) for comparison (Fig. 7 and Table 1). Fig. 7A shows the typical mass-normalized CV curves of USCS$_D$ Au$_{61.2}$@Au$_{27.3}$Pt$_{11.5}$-NP/C catalysts, commercial Pt/C catalysts and USCS Au$_{38.4}$@Au$_{9.3}$Pt$_{52.3}$-NP/C catalysts measured in the presence of N$_2$-saturated 0.25 M H$_2$SO$_4$ containing 1.0 M HCOOH at a sweep rate of 50 mV s^{-1}. Note that the mass-normalized CV curve of USCS Au$_{38.4}$@Au$_{9.3}$Pt$_{52.3}$-NP/C catalysts is also shown in Fig. S1 (ESI†) for a better comparison. One can see that, during the forward scan, a larger oxidation peak in the potential range of 0.0–0.6 V (vs. Ag/AgCl) can be observed in the

CV curve of USCS$_D$ Au$_{61.2}$@Au$_{27.3}$Pt$_{11.5}$-NP/C catalysts (the black curve in Fig. 7A), indicating that the FAOR occurs in the direct pathway (the dehydrogenation of formic acid).

In contrast, a weak peak in the potential range of 0.7–0.8 V (vs. Ag/AgCl) was observed in the CV curve of commercial Pt/C catalysts (the red curve in Fig. 7A). Furthermore, the CV curve of USCS Au$_{38.4}$@Au$_{9.3}$Pt$_{52.3}$-NP/C catalysts (the blue curve in Fig. 7A) is rather similar to that of commercial Pt/C catalysts, except the difference in their intensities. The results indicate the occurrence of dehydration in the FAOR (the indirect pathway) catalysed by both commercial Pt/C catalysts and USCS Au$_{38.4}$@Au$_{9.3}$Pt$_{52.3}$-NP/C catalysts.

In addition, the current density of USCS Au$_{38.4}$@Au$_{9.3}$Pt$_{52.3}$-NP/C catalysts is lower than that of commercial Pt/C catalysts, indicating that the performance of USCS Au$_{38.4}$@Au$_{9.3}$Pt$_{52.3}$-NP/C catalysts towards the FAOR is worse than that of commercial Pt/C catalysts. That is, the Pt-rich shell of USCS Au$_{38.4}$@Au$_{9.3}$Pt$_{52.3}$-NP/C catalysts cannot change the pathway of the FAOR and enhance the FAOR performance due to the great similarity between commercial Pt/C catalysts and USCS Au$_{38.4}$@Au$_{9.3}$Pt$_{52.3}$-NP/C catalysts. The difference in the oxidation potentials between the USCS$_D$ Au$_{61.2}$@Au$_{27.3}$Pt$_{11.5}$-NP/C catalysts, commercial Pt/C catalysts and USCS Au$_{38.4}$@Au$_{9.3}$Pt$_{52.3}$-NP/C catalysts (Fig. 7A and Table 1) also indicates that FAORs catalysed by them proceed through different pathways. Consequently, the Au-rich, discrete Pt shells of USCS$_D$ Au$_{61.2}$@Au$_{27.3}$Pt$_{11.5}$-NP/C catalysts indeed change the pathway of the FAOR and enhance the FAOR performance. Accordingly, the mass-normalized current density of USCS$_D$ Au$_{61.2}$@Au$_{27.3}$Pt$_{11.5}$-NP/C catalysts is about 6.91 A mg$_{Pt}^{-1}$, which is about 16.8 and 21.6 times higher than that (0.41 A mg$_{Pt}^{-1}$) of commercial Pt/C catalysts and that (0.32 A mg$_{Pt}^{-1}$) of USCS Au$_{38.4}$@Au$_{9.3}$Pt$_{52.3}$-NP/C catalysts, respectively (Fig. 7A and Table 1). When the mass of Au is also taken into account, the mass activity of USCS$_D$ Au$_{61.2}$@Au$_{27.3}$Pt$_{11.5}$-NP/C catalysts is about 0.79 A mg$_{metal}^{-1}$, which is still about 1.9 and 4.6 times higher than that (0.41 A mg$_{metal}^{-1}$) of commercial Pt/C catalysts and that (0.17 A mg$_{metal}^{-1}$) of USCS Au$_{38.4}$@Au$_{9.3}$Pt$_{52.3}$-NP/C catalysts, respectively. Moreover, the specific activity of USCS$_D$ Au$_{61.2}$@Au$_{27.3}$Pt$_{11.5}$-NP/C catalysts is about 4.88 mA cm^{-2},
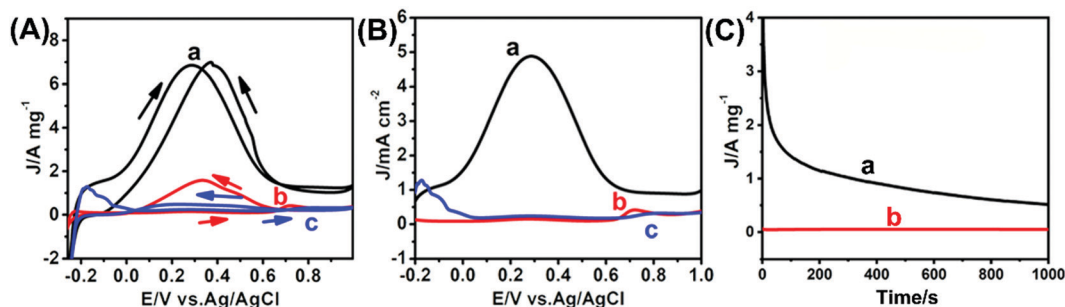

Fig. 7 CV curves (A and B) of USCS$_D$ Au$_{61.2}$@Au$_{27.3}$Pt$_{11.5}$-NP/C catalysts (a, black curve), commercial Pt/C catalysts (b, red curve) and USCS Au$_{38.4}$@Au$_{9.3}$Pt$_{52.3}$-NP/C catalysts (c, blue curve) in the presence of N$_2$-saturated 0.25 M H$_2$SO$_4$ containing 1.0 M HCOOH. The currents are normalized by Pt mass (A) and ECSA (B), respectively. The corresponding chronoamperometric tests (C) of USCS$_D$ Au$_{61.2}$@Au$_{27.3}$Pt$_{11.5}$-NP/C catalysts (a) and commercial Pt/C catalysts (b) were performed at a constant potential of 0.3 V (vs. Ag/AgCl).

Table 1 Summarized data of the electrocatalytic performance of USCS$_D$ Au$_{61.2}$@Au$_{27.3}$Pt$_{11.5}$-NP/C catalysts, commercial Pt/C catalysts and USCS Au$_{38.4}$@Au$_{9.3}$Pt$_{52.3}$-NP/C catalysts towards the FAOR in acidic media

Samples	Mass activity [A mg$_{Pt}^{-1}$]	Mass activity [A mg$_{metal}^{-1}$]	Specific activity [mA cm^{-2}]	Peak position [V vs. Ag/AgCl]
USCS$_D$ Au$_{61.2}$@Au$_{27.3}$Pt$_{11.5}$-NP/C catalysts	6.91	0.79	4.88	0.28
Commercial Pt/C catalysts	0.41	0.41	0.67	0.71
USCS Au$_{38.4}$@Au$_{9.3}$Pt$_{52.3}$-NP/C catalysts	0.32	0.17	0.32	0.82

which is about 7.3 and 15.3 times higher than that (0.67 mA cm^{-2}) of commercial Pt/C catalysts and that (0.32 mA cm^{-2}) of USCS Au$_{38.4}$@Au$_{9.3}$Pt$_{52.3}$-NP/C catalysts, respectively (Fig. 7B). Furthermore, the electrocatalytic performance in terms of the mass activity and specific activity of the as-prepared USCS$_D$ Au$_{61.2}$@Au$_{27.3}$Pt$_{11.5}$-NP/C catalysts towards the FAOR in acidic media is rather satisfactory compared with the Pt-based catalysts recently reported in the literature (Table S5, ESI†).

In addition to their catalytic activity, stability is also an important factor in their performance. Fig. 7C shows the results of chronoamperometric (CA) tests of USCS$_D$ Au$_{61.2}$@Au$_{27.3}$Pt$_{11.5}$-NP/C catalysts and commercial Pt/C catalysts, which were performed for 1000 s at a constant potential of 0.3 V (vs. Ag/AgCl) in the presence of N$_2$-saturated 0.25 M H$_2$SO$_4$ containing 1.0 M HCOOH. Generally, the sintering of electrocatalysts during the electrochemical measurements is unavoidable. This phenomenon is common to NP-based electrocatalysts, which would lead to variations in their outer surfaces. However, the outer surfaces of electrocatalysts gradually change during the electrochemical measurements. As for our USCS$_D$ Au$_{61.2}$@Au$_{27.3}$Pt$_{11.5}$-NP/C catalysts, the change in their outer surfaces should be similar to that of commercial Pt/C due to their comparable size. Accordingly, the mass-normalized current density of USCS$_D$ Au$_{61.2}$@Au$_{27.3}$Pt$_{11.5}$-NP/C catalysts also remarkably decreased at the initial stage of the chronoamperometric test. However, the decrease in the current density gradually becomes slow, possibly due to the formation of the Pt–Au alloy on their surfaces. One can clearly see that the current density of USCS$_D$ Au$_{61.2}$@Au$_{27.3}$Pt$_{11.5}$-NP/C catalysts is always higher than that of commercial Pt/C catalysts during the entire stability test. In addition, the final current density of USCS$_D$ Au$_{61.2}$@Au$_{27.3}$Pt$_{11.5}$-NP/C catalysts is also higher than the initial current density of commercial Pt/C catalysts. Thus, these results indicate that USCS$_D$ Au$_{61.2}$@Au$_{27.3}$Pt$_{11.5}$-NP/C catalysts display a higher long-term stability than commercial Pt/C catalysts.

4. Conclusions

In summary, USCS$_D$ Au–Pt NPs with discrete Pt shells were first successfully prepared by extending our previous method. It is found that USCS$_D$ Au$_{61.2}$@Au$_{27.3}$Pt$_{11.5}$ NPs are indeed different from USCS Au–Pt NPs based on the ECSA values, CO stripping voltammograms and XPS data. Moreover, the as-prepared USCS$_D$ Au$_{61.2}$@Au$_{27.3}$Pt$_{11.5}$-NP/C catalysts towards the FAOR

proceed through the direct pathway (dehydrogenation) which can effectively avoid the poisoning of intermediate products and produce hydrogen through the direct route. Furthermore, the mass activity and specific activity of the as-prepared USCS$_D$ Au$_{61.2}$@Au$_{27.3}$Pt$_{11.5}$-NP/C catalysts towards the FAOR are 6.91 A mg$_{Pt}^{-1}$ and 4.88 mA cm^{-2}, which are about 16.8 and 7.33 times higher than those (0.4 A mg$_{Pt}^{-1}$ and 0.67 mA cm^{-2}) of commercial Pt/C catalysts, respectively. In addition, they also show a better long-term stability. Our results demonstrate that our synthetic strategy indeed can be extended to directly prepare ultra-small Au-based bimetallic NPs via a one-pot reaction as electrocatalysts for application in energy storage and conversion.

Conflicts of interest

There are no conflicts to declare.

Acknowledgements

References

1 M. A. Ahsan, A. R. P. Santiago, Y. Hong, N. Zhang, M. Cano, E. Rodriguez-Castellon, L. Echegoyen, S. T. Sreenivasan and J. C. Noveron, J. Am. Chem. Soc., 2020, 142, 14688–14701.

2 P. Li, C. Du, X. Gao, Z. Zhuang, D. Xiang, C. Zhang and W. Chen, Nanoscale, 2020, 12, 13688–13696.

3 X. X. Wang, J. Sokolowski, H. Liu and G. Wu, Chin. J. Catal., 2020, 41, 739–755.

4 Y. Cao, Y. Xiahou, L. Xing, X. Zhang, H. Li, C. Wu and H. Xia, Nanoscale, 2020, 12, 20456–20466.

5 A. Cuesta, G. Cabello, M. Osawa and C. Gutierrez, ACS Catal., 2012, 2, 728–738.

6 G. Samjeske, A. Miki, S. Ye and M. Osawa, J. Phys. Chem. B, 2006, 110, 16559–16566.

7 Y. Yu, X. Wang and K. H. Lim, Catal. Lett., 2011, 141, 1872–1882.

8 R. V. Niquirilo, E. Teixeira-Neto, G. S. Buzzo and H. B. Suffredini, Int. J. Electrochem. Sci., 2010, 5, 344–354.

9 M. Ahn and J. Kim, J. Phys. Chem. C, 2013, 117, 24438–24445.

10 C. Wu, H. Li, H. He, Y. Song, C. Bi, W. Du and H. Xia, ACS Appl. Mater. Interfaces, 2019, 11, 46902–46911.

11 Y. J. Jang, J.-W. Jang, J. Lee, J. H. Kim, H. Kumagai, J. Lee, T. Minegishi, J. Kubota, K. Domen and J. S. Lee, *Energy Environ. Sci.*, 2015, **8**, 3597–3604.

12 Y. Hori, H. Wakebe, T. Tsukamoto and O. Koga, *Electrochim. Acta*, 1994, **39**, 1833–1839.

13 J. Jia, L. Cao and Z. Wang, *Langmuir*, 2008, **24**, 5932–5936.

14 J. Luo, M. M. Maye, N. N. Kariuki, L. Y. Wang, P. Njoki, Y. Lin, M. Schadt, H. R. Naslund and C. J. Zhong, *Catal. Today*, 2005, **99**, 291–297.

15 L. Lu, Y. Nie, Y. Wang, G. Wu, L. Li, J. Li, X. Qi and Z. Wei, *J. Mater. Chem. A*, 2018, **6**, 104–109.

16 M. Eyrich, T. Diemant, H. Hartmann, J. Bansmann and R. J. Behm, *J. Phys. Chem. C*, 2012, **116**, 11154–11165.

17 W. Ye, H. Kou, Q. Liu, J. Yan, F. Zhou and C. Wang, *Int. J. Hydrogen Energy*, 2012, **37**, 4088–4097.

18 D. Li, F. Meng, H. Wang, X. Jiang and Y. Zhu, *Electrochim. Acta*, 2016, **190**, 852–861.

19 S. Zhang, Y. Shao, G. Yin and Y. Lin, *J. Power Sources*, 2010, **195**, 1103–1106.

20 Y.-H. W. Dan Zhao and B.-Q. Xu, *J. Phys. Chem. C*, 2009, **113**, 20903–20911.

21 C. Li, Y. Xu, H. Yu, K. Deng, S. Liu, Z. Wang, X. Li, L. Wang and H. Wang, *Nanotechnology*, 2020, **31**, 045401.

22 X. Jiang, X. Yan, W. Ren, Y. Jia, J. Chen, D. Sun, L. Xu and Y. Tang, *ACS Appl. Mater. Interfaces*, 2016, **8**, 31076–31082.

23 X. Hu, J. Zou, H. Gao and X. Kang, *J. Colloid Interface Sci.*, 2020, **570**, 72–79.

24 W. Z. Wang, B. Poudel, Y. Ma and Z. F. Ren, *J. Phys. Chem. B*, 2006, **110**, 25702–25706.

25 C. Zhang, L. Xu, N. Shan, T. Sun, J. Chen and Y. Yan, *ACS Catal.*, 2014, **4**, 1926–1930.

26 P. Tonda-Mikiela, T. W. Napporn, C. Morais, K. Servat, A. Chen and K. B. Kokoh, *J. Electrochem. Soc.*, 2012, **159**, H828–H833.

27 S. Strbac, S. Petrovic, R. Vasilic, J. Kovac, A. Zalar and Z. Rakocevic, *Electrochim. Acta*, 2007, **53**, 998–1005.

28 A. Habrioux, E. Sibert, K. Servat, W. Vogel, K. B. Kokoh and N. Alonso-Vante, *J. Phys. Chem. B*, 2007, **111**, 10329–10333.

29 A. Habrioux, W. Vogel, M. Guinel, L. Guetaz, K. Servat, B. Kokoh and N. Alonso-Vante, *Phys. Chem. Chem. Phys.*, 2009, **11**, 3573–3579.

30 T. Miao, Y. Song, C. Bi, H. Xia, D. Wang and X. Tao, *J. Phys. Chem. C*, 2015, **119**, 18434–18443.

31 C. Bi, C. Feng, T. Miao, Y. Song, D. Wang and H. Xia, *Nanoscale*, 2015, **7**, 20105–20116.

32 A. J. Wang, K.-J. Ju, Q.-L. Zhang, P. Song, J. Wei and J.-J. Feng, *J. Power Sources*, 2016, **326**, 227–234.

33 W. Ye, J. Yu, Y. Zhou, D. Gao, D. Wang, C. Wang and D. Xue, *Appl. Catal., B*, 2016, **181**, 371–378.

34 P. Wu, Y. Cao, Y. Wang, W. Xing, Z. Zhong, P. Bai and Z. Yan, *Appl. Surf. Sci.*, 2018, **457**, 580–590.

© 2022 The Author(s). Published by the Royal Society of Chemistry